Tribology International 218 (2026) 111762

Contents lists available at ScienceDirect

Tribology International

journal homepage: www.elsevier.com/locate/triboint

Full Length Article

# Modeling with experimental validation of power loss in high-speed rolling bearings with oil-jet lubrication for helicopter transmission systems

Pengfei Zhou, Jie Ling *, Ruifeng Zhao

*College of Mechanical and Electrical Engineering, Nanjing University of Aeronautics and Astronautics, 29 Yudao Street, Nanjing, 210016, China*

ARTICLE INFO

*Keywords:*
Helicopter
High-speed transmission
Rolling bearings
Oil injection lubrication
Power loss

ABSTRACT

Targeting the critical need for efficiency and thermal management in helicopter transmission systems, this study focuses on the power loss of high-speed rolling bearings under oil-jet lubrication — a dominant lubrication method in such systems. To address this issue, this paper establishes a localized mathematical model for predicting the power loss of rolling bearings under oil-jet lubrication. The model's completeness is enhanced by incorporating two key mechanisms: the dynamic load effect on rolling elements at high speeds and the oil shear drag loss at the bearing inlet interface. Based on this model, the power losses of several typical bearing types under identical operating conditions with low radial load are calculated. To validate the model, a dedicated test rig was built to conduct oil-jet lubrication experiments under the same low-load condition. Although this specific loading condition imposes certain limitations on the model's applicability, the experimental results can still be used for model verification. The results show that the theoretical predictions agree well with the experimental data in overall trend. Further analysis reveals the variation patterns of individual loss sources with rotational speed, particularly the contribution proportion of the newly introduced power loss terms, thereby validating the correctness and necessity of the supplemented mechanisms. This study provides a generalized model and a theoretical basis for optimal bearing selection and loss suppression, directly supporting efficiency improvements in helicopter transmissions.

## 1. Introduction

As a core component for power transmission, the reliability, efficiency, and service life of a helicopter's transmission system directly affect the overall performance and safety of the aircraft. The main heat sources within the system originate from high-speed gears and bearings, where friction-induced heat and power loss become especially significant under high-load and high-speed operating conditions. Therefore, effective lubrication is essential to ensure the system functions properly. Lubrication not only performs the fundamental functions of reducing friction and wear but also plays a critical role in enhancing heat exchange, controlling temperature rise, and optimizing transmission performance. Among the lubrication methods for rolling element bearings, under-ring lubrication and oil-jet lubrication are two typical techniques [1–4]. oil-jet lubrication, characterized by a simple structural design, thorough lubrication, and excellent cooling effect, is widely used in rolling element bearings within helicopter transmission systems. Despite these advantages, the power losses associated with oil-jet lubrication cannot be overlooked. Significant energy consumption occurs during oil injection, agitation, and circulation due to fluid shear, oil-air entrainment, and impact effects, thereby reducing the overall efficiency of the helicopter's transmission system. Furthermore, friction effects in high-speed rolling element bearings [5,6] also contribute considerably to power loss, adversely affecting service life and potentially leading to bearing failure. Thus, to control inefficient power losses in high-speed rolling element bearings during lubrication, it is necessary to accurately model the power loss sources of each component.

As critical components in transmission systems, the power loss of rolling bearings directly impacts system efficiency, temperature rise, and reliability, particularly under high-speed, heavy-load, or lubrication-limited conditions. In recent years, significant progress has been made in the theoretical modeling, numerical simulation, and experimental validation of power loss in rolling bearings. To predict bearing power loss, early research efforts primarily relied on global empirical models. Notable examples include the classic Harris–Palmgren model [7,8] and the SKF model [9]. These models provide a straightforward estimate of total bearing power loss based on operational parameters. However, their accuracy heavily depends on extensive calibration with experimental data, and they offer limited physical insight into the contributions of different loss mechanisms. To overcome these limitations and achieve more refined predictions, research

* Corresponding author.
*E-mail address:* meejling@nuaa.edu.cn (J. Ling).

https://doi.org/10.1016/j.triboint.2026.111762
Received 24 October 2025; Received in revised form 15 January 2026; Accepted 25 January 2026
Available online 27 January 2026

gradually shifted towards localized analytical modeling. This approach decomposes the total power loss into distinct physical sources, quantifying each separately. For instance, Veauce D et al. [10] established a localized drag loss model for oil-bath lubricated Deep Groove Ball Bearings (DGBBs) that accounts for oil level variations, significantly enhancing predictive accuracy. L. Darul et al. [11,12] systematically investigated the significant contribution (up to 40% of total loss) from unloaded rolling elements in the iso-viscous rigid lubrication regime under low loads and successfully extended this model to Angular Contact Ball Bearings (ACBBs) [13], confirming hydrodynamic rolling as the dominant loss source under oil-jet lubrication. For Tapered Roller Bearings (TRBs), R. S. Zhou et al. [13] proposed a torque prediction model based on elastohydrodynamic lubrication theory and micro–macro contact analysis.

The advancement of localized modeling naturally led to a more refined categorization of power loss physics, typically based on their correlation with external load. Power losses are distinctly categorized into load-dependent and load-independent types [7,8]. Load-dependent losses primarily arise from sliding friction directly caused by contact loads. At high speeds, the centrifugal force on rolling elements significantly alters the internal load distribution, affecting these losses. Jones [6] systematically analyzed the sliding friction mechanism in ball bearings, while Zhao et al. [5] further integrated rolling–sliding contact into their ball bearing power loss model. For Cylindrical Roller Bearings (CRBs), Rivera G et al. [14] proposed an improved analytical model for sliding friction torque by decomposing the differential sliding caused by roller spin and orbital motion. In contrast, load-independent losses originate primarily from fluid dynamic effects induced by the lubricant, including drag losses on rolling elements and the cage, cage churning loss, and injection loss [10,11,15]. These losses often dominate under high-speed or ample lubrication conditions. Peterson et al. [15], for example, demonstrated the significant presence and sensitivity of fluid drag loss in DGBBs and needle roller bearings to lubrication conditions.

To further reveal the complex internal flow mechanisms behind these load-independent losses, Computational Fluid Dynamics (CFD) has emerged as a powerful tool. CFD enables direct simulation of complex oil-air two-phase flow and energy dissipation within the bearing chamber, overcoming limitations of theoretical models in describing local flow fields. Peterson et al. [15], through CFD and experimental comparison, indicated that optimizing lubrication conditions and bearing type is more effective in reducing fluid drag than improving cage design. Feldermann et al. [16] developed a CFD method for efficient analysis of loss distribution in radial CRBs. Liebrecht et al. [17] used CFD to study fluid drag loss in TRBs, finding only partial consistency with empirical models. The applicability of numerical methods themselves has also been explored; Zhao et al. [18] compared the Finite Volume Method (FVM) and the Moving Particle Semi-implicit (MPS) method for predicting churning loss. Furthermore, Marchesse et al. [19] employed a CFD approach to investigate drag power loss in cylindrical roller bearings, while Maccioni et al. [20] developed a multiphase CFD solver to study lubricant behavior in partially flooded tapered roller bearings. For oil-jet lubrication specifically, Hu et al. [21] simulated two-phase flow fields under different nozzle angles using the Volume of Fluid (VOF) method, demonstrating CFD's advantage in detailing lubrication supply characteristics.

Building upon the fundamental understanding provided by analytical and numerical models, recent research has focused on lubrication optimization and integrated analysis for specific applications. For helicopter transmission systems, Chen J et al. [22] conducted multi-objective optimization of lubrication parameters for planetary gear bearings. For machine tool spindle systems, Kim K S et al. [23] integrated bearing analysis with thermal analysis to predict friction torque and temperature distribution. Furthermore, systematic reviews [24] and studies considering component flexibility [25], oil-air two-phase flow characteristics [26,27] highlight the ongoing effort to enhance model completeness and practical relevance.

Despite significant progress, several key shortcomings remain in predicting power loss for high-speed rolling bearings under oil-jet lubrication, particularly under the low-load conditions often encountered in helicopter transmissions. First, many models are developed for specific bearing series, lacking a unified framework with broad applicability. Second, existing studies often rely on quasi-static assumptions, failing to fully account for the influence of high-speed dynamic loads on rolling element loads and subsequent power loss. Third, the oil film shear loss at the lubrication inlet region is frequently simplified or neglected, although it may contribute significantly at high rotational speeds.

These research gaps are particularly critical for helicopter transmission systems, where high-speed rolling bearings must operate reliably under low radial loads with oil-jet lubrication. The accurate prediction of bearing power loss in this context is essential for optimizing transmission efficiency and thermal management. Therefore, addressing these limitations is not only of academic interest but also of direct practical significance for helicopter transmission design and bearing selection.

To address these research gaps, this study develops a generalized modeling framework for bearing power loss under limited radial load conditions. The framework is structured around three key contributions:

- A Unified Loss-Source Consolidation: Power dissipation mechanisms are systematically categorized and quantified. Mechanisms with similar physical properties are consolidated into unified sub-models to enhance the model's applicability across different bearing types.
- High-Speed Dynamic Load Modeling: A dedicated model for the dynamic effects on rolling element loads under high-speed conditions is introduced. While negligible at medium-to-low speeds, these loads significantly impact total power loss at high speeds due to enhanced inertial effects, a phenomenon that warrants in-depth analysis.
- Oil Shear Drag Physics at the Inlet: A physical model is developed specifically for oil shear drag losses at the bearing's oil inlet interface, a critical yet often simplified mechanism.

Collectively, this work provides a theoretical foundation for more comprehensive and dynamic predictions of bearing power loss, supporting optimal bearing selection and the reduction of inefficient energy dissipation in helicopter transmission systems.

The remaining is organized as follows. Section 2 systematically categorizes power loss models of the same type across various bearings and incorporates power loss mechanisms not sufficiently considered in existing studies, thereby integrating a theoretical modeling framework with general applicability for bearing power loss. Section 3 involves the design and construction of a dedicated bearing test rig. Under conditions without external radial load, oil injection lubrication experiments were conducted on DGBBs, CRBs, and TRBs. The averaged results from multiple experimental measurements were compared with the theoretical model proposed in the first part for comparative validation and accuracy assessment. On this basis, further analysis was carried out in Section 4 to examine the contribution of the supplemented power loss sources to the total power loss as a function of rotational speed, as well as the variation trends of various types of loss sources with speed. The conclusions are finally made in Section 5.

## 2. Analytical model

This section introduces a universal power loss model aimed at systematically integrating power loss mechanisms across diverse bearing types. Through a localized modeling methodology, the total power loss is decomposed into four constituent elements: dragging loss, sliding friction loss, injection loss, and cage churning loss.

It is worth noting that the proposed model is developed and validated for rolling bearings operating under specific conditions: high

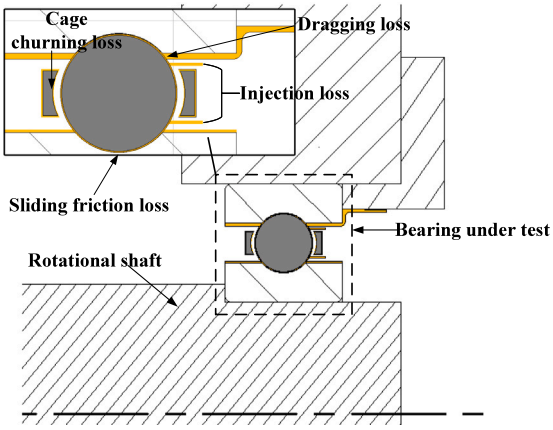


**Fig. 1.** Schematic diagram of different loss sources.

rotational speeds (up to 6000 rpm), low radial loads (less than 5% of the dynamic load rating), and oil-jet lubrication. While the primary application context motivating this study is helicopter transmission systems, the model framework is general and applicable to other high-speed machinery where bearings operate under similar low-load, oil-jet lubricated conditions.

As shown in Fig. 1, the diagram presents the four sources of power loss in rolling bearings under oil jet lubrication conditions with limited radial load. These include: Dragging loss, generated by the interaction between rolling elements and the oil, as well as between bearing surfaces and the oil; Sliding friction loss, arising from the interaction between rolling elements and raceways; Injection loss, caused by the interaction of the oil jet with rolling elements and the cage; Cage churning loss, resulting from the interaction between the cage and the oil.

### 2.1. Dragging loss

#### 2.1.1. Dragging loss on rolling element

Hydrodynamic drag loss refers to the energy dissipation caused by the motion of an object through a fluid, primarily resulting from viscous effects and kinetic energy loss. The drag loss generated by an isolated sphere moving in an unbounded medium can be expressed as [28]:

$$P_{\mathrm{d}} = \frac{1}{2}\rho A C_{\mathrm{D}} u^3 \tag{1}$$

where $\rho$ represents the density of the fluid medium, $A$ denotes the projected area of the rolling element perpendicular to the flow, and $u$ is the velocity of the rolling element. $C_{\mathrm{D}}$ is the drag coefficient, which depends on the shape of the rolling element and the Reynolds number, as shown in Eqs. (3) and (4). Re is defined as follows:

$$\mathrm{Re} = \frac{\rho v L}{\mu} \tag{2}$$

where $L$ ($L$ does not involve infinitely long rollers) represents the characteristic length (for DGBBs, the ball diameter; for CRBs, the length of the roller generatrix; for TRBs, the vertical distance from the large end to the small end of the roller), $v$ denotes the velocity of motion, and $\mu$ represents the dynamic viscosity.

Through systematic experimental investigations, Schlichtig [29] established empirical correlations between the drag coefficient ($C_{\mathrm{D}}$) and the Reynolds number for both spherical and cylindrical objects. To preserve completeness of the data, as shown in Fig. 2, this study plots the relationship curve based on the original experimental data and applies an interpolation method to process the aforementioned data to estimate the drag coefficient under corresponding operating conditions.

Based on experimental data, fitting was performed to derive expressions for the drag coefficient of spherical and cylindrical objects within the Reynolds number range of $0.1 \le \mathrm{Re} \le 10^5$. Expression for spherical rollers as follows:

$$C_{\mathrm{D}} = \begin{cases} \frac{\mathrm{Re}}{24}, & \mathrm{Re} < 1 \\ \frac{24}{\mathrm{Re}}(1 + 0.25\mathrm{Re}^{0.7}) + \frac{0.3}{1+K\mathrm{Re}^{-1.8}}, & 1 \le \mathrm{Re} < 1000 \\ 0.42, & \mathrm{Re} \ge 1000 \end{cases} \tag{3}$$

where $K = 5 \times 10^4$.

Expression for cylindrical rollers as follows:

$$C_{\mathrm{D}} = \begin{cases} 10.0 - K_1 \lg(\mathrm{Re}) & \mathrm{Re} \le 10 \\ 10^{\left(K_2(\lg(\mathrm{Re}))^2 - K_3 \lg(\mathrm{Re}) + 0.85\right)} & 10 < \mathrm{Re} \le 1000 \\ 1.14 & \mathrm{Re} > 1000 \end{cases} \tag{4}$$

where $K_1 = 0.72$, $K_2 = 0.05$, $K_3 = 0.45$.

Under oil-jet lubrication conditions, the rolling elements in a bearing operate within an oil-air mixture medium. This mixture can be treated as a homogeneous phase, whose physical and rheological properties are primarily determined by the oil volume fraction. Among these properties, the effective density $\rho_{\mathrm{e}}$ and the effective dynamic viscosity $\eta_{\mathrm{e}}$ serve as key parameters characterizing the behavior of the mixed medium, as shown in the following equation:

$$\rho_{\mathrm{e}} = \rho_{\mathrm{oil}} X + \rho_{\mathrm{air}}(1 - X) \tag{5}$$

$$\eta_{\mathrm{e}} = \left(\frac{(1 - X_m)}{\eta_{\mathrm{air}}} + \frac{X_m}{\eta_{\mathrm{oil}}}\right)^{-1} \tag{6}$$

where $X_m$ depends on whether an oil ring is formed during bearing operation. The formation of the oil ring, in turn, is determined by whether the oil volume $V$ inside the bearing cavity exceeds its critical volume $V_{\mathrm{crit}}$, which can be calculated according to the following formula proposed in Refs. [10,30]:

$$V_{\mathrm{crit}} = \pi(d_o^2 - d_i^2)B/4 \tag{7}$$

$$V = V_s + V_{in} - V_{out} \tag{8}$$

where $d_o$ and $d_i$ represent the diameters of the outer and inner raceways of the bearing, respectively, $B$ denotes the bearing width, $V_{\mathrm{in}}$ is the volumetric inflow rate of the lubricant, and $V_{\mathrm{out}}$ refers to the volumetric outflow rate. Under given operating conditions, the lubrication state of the rolling bearing will eventually reach a dynamic equilibrium where $V_{\mathrm{in}}$ equals $V_{\mathrm{out}}$. Under this condition, the following relationship holds:

$$V = V_s \tag{9}$$

where $V_s$ denotes the quasi-static oil volume. When the oil volume $V$ in the bearing cavity exceeds the critical volume $V_{\mathrm{crit}}$, the medium density is taken as $\rho = \rho_{\mathrm{oil}}$; when $V$ is less than $V_{\mathrm{crit}}$, the effective density $\rho = \rho_{\mathrm{eff}}$ is used. Based on (1), the drag loss acting on the rolling elements in the bearing can be expressed as:

$$P_{\mathrm{d}} = \frac{1}{2} Z \rho_{\mathrm{e}} C_D A \left(\omega_c \frac{d_m}{2}\right)^3 \tag{10}$$

where $Z$ is the number of rolling elements, $\omega_c$ represents the rotational speed of the cage, and $d_m$ denotes the pitch diameter of the bearing.

#### 2.1.2. Dragging loss of external lubrication

Under the combined action of inertial and centrifugal forces, complex fluid interactions occur at the interface between the oil inlet and the bearing chamber, manifesting macroscopically as shearing behavior between the surrounding oil and the chamber wall. Theoretically, the lubricant in this region exhibits not only circumferential motion but is also influenced by axial entrainment effects. However, in this study, to simplify the computational model, the influence of axial entrainment on the overall oil movement is deliberately neglected, and quantitative calculations are performed exclusively for the power loss caused by circumferential shearing.

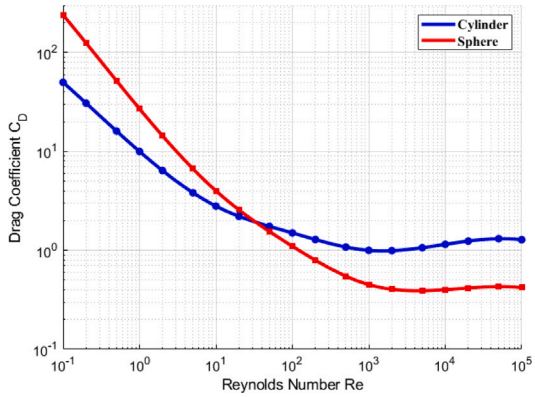


**Fig. 2.** Dependence of the drag coefficient on the Reynolds number.

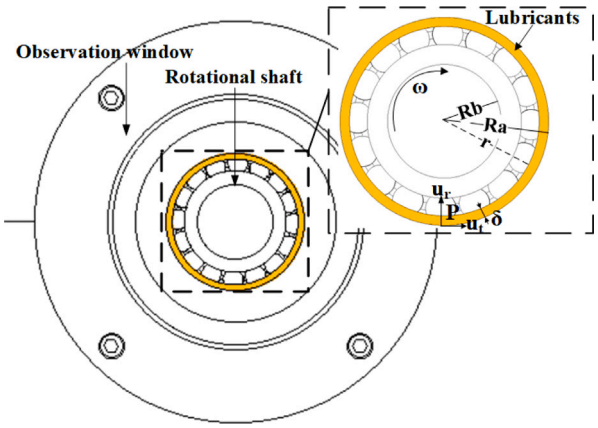


**Fig. 3.** Schematic diagram of tangential flow in peripheral oil.

Based on Fig. 3, $R_a$ denotes the radius of the outer wall of the bearing chamber, $R_b$ represents the radius of the inner race; $u_t$ and $u_r$ indicate the tangential and radial velocity components of the lubricating medium, respectively, and $P$ refers to the pressure field distribution within the lubricating medium.

To render the governing equations analytically solvable while maintaining a reasonable degree of physical realism and to achieve appropriate simplification for the flow mechanisms of interest in this study, thereby highlighting the core influencing factors. The following fundamental assumptions are introduced:

- The lubricating medium is in a steady-state flow condition;
- The pressure of the lubricating medium varies only in the radial direction;
- The lubricating medium is an incompressible fluid;
- The radial velocity component of the lubricating medium is zero.

Thus, the tangential velocity is then given by the following expression [31]:

$$u_t = \frac{\omega_c R_a^2}{R_a^2 - R_b^2}\left(r - \frac{R_b^2}{r}\right) \tag{11}$$

The boundary conditions used in the equation are as follows: $r = R_a, u_t = \omega_c R_a$; $r = R_b, u_t = 0$. Based on Eq. (11), the power loss due to peripheral oil shearing is then calculated using the following formula:

$$P_t = b_o \rho_{\text{oil}} R_a \omega_c^3 \left(\frac{R_a^2}{R_a^2 - R_b^2}\right)^2 \int_{R_a-\delta}^{R_a}\left(r - \frac{R_b^2}{r}\right)^2 dr \tag{12}$$

where $b_o$ denotes the width of the peripheral oil ring, and $\delta$ is determined by the following expression:

$$\delta = \sqrt{\frac{12\mu}{\rho_{\text{oil}}\omega_c}}, \tag{13}$$

### 2.2. Sliding friction loss

In ball bearings, sliding friction primarily occurs between the rolling elements and the raceways. In contrast, for cylindrical and TRBs, in addition to the friction between the rolling elements and raceways, significant sliding friction also arises between the roller ends and the guide ribs when axial loads are applied. Prior studies [6,8,13] have systematically analyzed the load distribution in different types of bearings. Under the condition of limited radial load only, this study further incorporates the influence of centrifugal forces of the rolling elements, while the gyroscopic moment effect is neglected, to refine the friction loss model under such working conditions. The centrifugal force acting on a rolling element is estimated by the following expression:

$$F_c = \frac{1}{2} m d_m \omega_c^2 \tag{14}$$

where $m$ denotes the mass of the rolling element, $d_m$ represents the pitch diameter of the bearing, and $\omega_c$ signifies the rotational speed of the cage.

#### 2.2.1. Rolling contact friction losses

Under the assumption of a constant friction coefficient, the sliding force at each rolling element-raceway contact can be estimated by the following expression:

$$F_{sj} = \mu_s (Q_{nj} + F_c) \tag{15}$$

where the sliding friction coefficient $\mu_s$ is taken as 0.07 [6]; $Q_{nj}$ denotes the normal load distributed on the jth rolling element under radial load, which is calculated according to the method described in Ref. [11]. Based on Eq. (15), the frictional power loss between the rolling elements and the raceways can be estimated by the following expression:

$$P_s = \sum_{j=1}^{Z} F_{sj}(v_{soj} + v_{sij}) \tag{16}$$

where the value of $v_s$ can be estimated based on the method proposed by Harris [8]; the subscripts $o$ and $i$ correspond to the outer raceway and inner raceway, respectively.

#### 2.2.2. Side-wall friction loss

In CRBs, when subjected to an axial load, an elliptical contact zone forms between the roller ends and the guiding flanges to balance this axial force. The high contact stress within this zone is the primary cause of the associated frictional loss. In this study, which focuses on conditions without applied axial load and no axial preload, the rollers remain properly aligned, and therefore the associated frictional loss is negligible [8]. In contrast, for TRBs under steady-state operating conditions, the rolling elements can be assumed to be in force equilibrium, with the corresponding mechanical analysis model illustrated in Fig. 4

$$Q_i \cos\alpha_i - Q_o \cos\alpha_o - Q_f \cos\alpha_f = 0 \tag{17}$$

$$Q_i \sin\alpha_i - Q_o \sin\alpha_o - Q_f \sin\alpha_f = F_c \tag{18}$$

where $Q_i$ denotes the contact load between the inner raceway and the roller, $Q_o$ represents the contact load between the outer raceway and the roller, $Q_f$ indicates the contact load between the large end of the roller and the guide flange, and $F_c$ is the centrifugal force acting on the roller; $\alpha_i$ is the contact angle of the inner raceway, $\alpha_o$ the contact angle of the outer raceway, and $\alpha_f$ the inclination angle of the

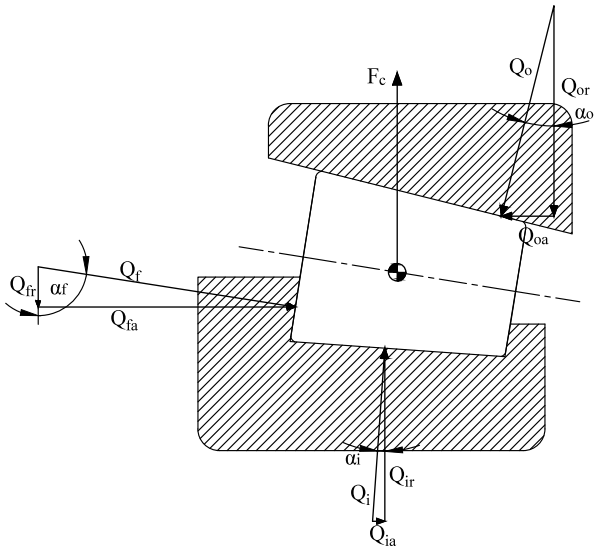


**Fig. 4.** Schematic diagram of the mechanical analysis of a TRB under the influence of centrifugal force.

flange contact. The contact load $Q_o$ between the outer raceway and the roller is determined by the radial load. Based on $Q_o$, the contact load $Q_f$ between the large end of the roller and the guide flange can be expressed as a function of $Q_o$ as follows :

$$Q_f = \frac{Q_o \sin(\alpha_i - \alpha_o) - F_c \cos\alpha_i}{\sin(\alpha_f - \alpha_i)} \tag{19}$$

Therefore, the sliding friction force in the flange contact zone can be calculated based on the method proposed in Ref. [32]:

$$F_f = \mu_f Q_f \tag{20}$$

where $\mu_f$ is the friction coefficient in the sliding zone, the value of which is determined according to Ref. [13]. The frictional power loss generated in the contact zone between the large end of the roller and the guide flange can be estimated by the following expression:

$$P_f = M_f \omega_c \tag{21}$$

where $\omega_c$ is the angular velocity of the cage. Based on this, the frictional torque $M_f$ generated between the large end of the roller and the guide flange can be calculated according to the method proposed in Ref. [33] using the following formula:

$$M_f = \sum_{j=1}^{Z} \left( F_f \frac{R_t}{D_t} h_f + \frac{M_p}{D_t} R_t \right) \tag{22}$$

where $R_t$ is the effective radius of curvature in the direction of lubricant entrainment, $D_t$ is mean roller diameter, $h_f$ is $M_p$ is the contact height, determined based on the method provided in Ref. [33].

### 2.3. Injection loss

During the oil-jet lubrication process of rolling bearings, the lubricant is typically injected from the side at a certain angle $\theta$ relative to the rotational direction of the bearing. The jet impinges on the region near the cage at a specific incidence angle. During this impact, most of its kinetic energy in the original injection direction is rapidly dissipated. As the bearing continues to operate, the impacted jet is subjected to viscous shear effects and subsequently moves circumferentially along with the cage and rolling elements, neglecting the influence of gravity. Given the high-speed operational characteristics of this bearing, the research employs an oil-jet lubrication mechanism where lubricant is directly injected onto the ball surfaces through small-diameter nozzles, as illustrated in Fig. 5.

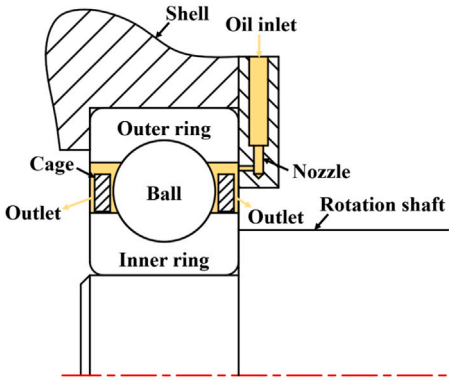


**Fig. 5.** Schematic diagram of oil injection lubrication method of bearings.

According to the fluid momentum theorem, the following expression can be derived:

$$F_j = \dot{m} V_j \cos\theta \tag{23}$$

where $V_j$ is the injection velocity of the lubricant, and $\dot{m}$ denotes the mass flow rate of the lubricant, which can be calculated by the following formula:

$$\dot{m} = \rho_{\text{oil}} Q_j \tag{24}$$

where $Q_j$ denotes the oil injection flow rate. Based on this parameter, the power loss induced by oil-jet impact can be calculated by the following expression:

$$P_{\text{j}} = \eta F_{\text{j}} \omega_c \left( \frac{d_m}{2} \right) \tag{25}$$

where $\eta$ can be estimated from Ref. [34], $F_{\text{j}}$ defined in Eq. (23), $\theta = 0°$, as shown in Fig. 5.

### 2.4. Cage churning loss

When the cage rotates within the lubricating medium, its interaction with the fluid results in power loss in the bearing [15,35], which is generally categorized as “cage churning loss”. Physically, such loss originates primarily from the viscous shear stresses generated by the fluid on the moving surfaces. On surfaces such as the cylindrical and end faces of the cage, where the normal direction is perpendicular to the velocity direction, pressure forces do no work; therefore, the core component of cage churning loss is viscous shear loss. Accordingly, this section will separately establish models for the viscous shear loss on the cylindrical surface and the end faces of the cage. Furthermore, although highly dynamic contacts also exist between the rolling elements and the cage, the extremely low load in this contact region results in frictional behavior that differs significantly from the high-load contacts between the rolling elements and raceways. Therefore, the contribution of this mechanism is generally neglected in power loss calculations.

#### 2.4.1. Churning loss on cylindrical surface of the cage

The churning power loss on the cylindrical surface of the cage can be estimated by the following expression:

$$P_c = \frac{1}{2} f \rho_{\text{e}} A_c \omega_c^3 \left( \frac{d_m}{2} \right)^3 \tag{26}$$

where $A_c$ is the projected area of the cage, $\rho_{\text{e}}$ denotes the equivalent density of the lubricating medium, and $d_m$ represents the pitch diameter of the bearing; $f$ is the flow regime correlation factor, the value of which depends on the type of flow state of the lubricating medium and can be determined according to Ref. [35].

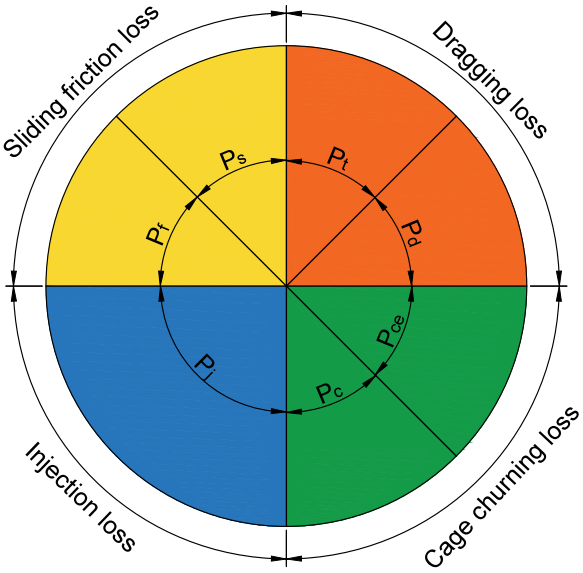


**Fig. 6.** Schematic diagram of power loss contributions (the scope does not represent the proportion of total power).

#### 2.4.2. Churning loss on end face of the cage

The power loss generated by the end faces of the cage can be estimated using the following expression [35]:

$$P_{ce} = \frac{1}{2}\rho_e \omega_c^3 R^5 f_n \tag{27}$$

In Eq. (27), $f_n$ can be calculated using the following expression:

$$f_n = \begin{cases} 3.87/\mathrm{Re}^{0.50} & \mathrm{Re} < 300\,000 \\ 0.146/\mathrm{Re}^{0.20} & \mathrm{Re} > 300\,000 \end{cases} \tag{28}$$

where Re can be calculated with reference to Eq. (2).

In Eq. (27), $R$ denotes the effective radius of the cage. It can be obtained from the following expression [36]:

$$R^5 = \begin{cases} r_{co}(r_{co}^4 - r_{ci}^4) & \text{for laminar flow} \\ r_{co}^{0.40}(r_{co}^{4.60} - r_{ci}^{4.60}) & \text{for turbulent flow} \end{cases} \tag{29}$$

where $r_{co}$ and $r_{ci}$ denote the outer diameter and inner diameter of the cage, respectively.

### 2.5. Summary

Fig. 6 illustrates the overall framework of the localized power loss model established in this study. The total power loss is systematically decomposed into four primary physical mechanisms, which are further refined into seven specific terms that can be calculated through independent sub-models. Each term corresponds to the equations provided in the main text. Based on the foregoing derivations, the total power loss can be expressed as follows:

$$P = P_\mathrm{d} + P_t + P_s + P_f + P_\mathrm{j} + P_c + P_{ce} \tag{30}$$

## 3. Experiments

### 3.1. Test bench

To validate the accuracy of the theoretical model, this study designed and developed a high-speed bearing oil injection and return test rig. Fig. 7(a) presents a physical photograph of the test setup. The test bearing is mounted inside a sealed chamber, where a preload is applied through a dedicated bearing housing to achieve precise control

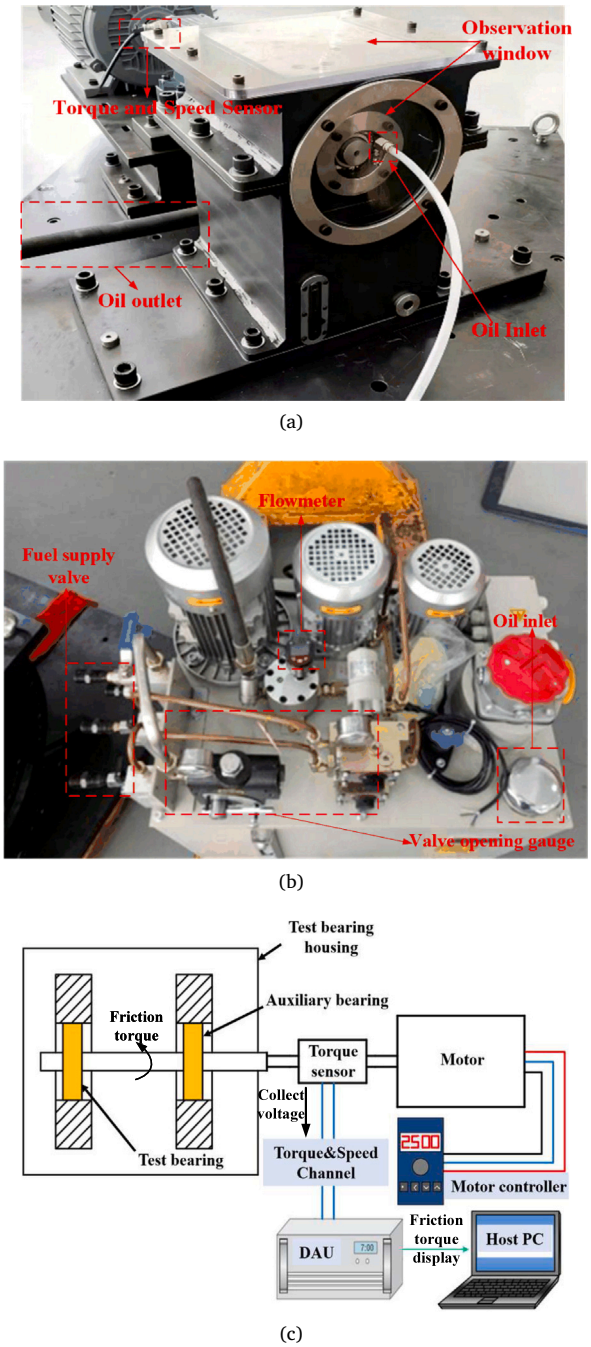


**Fig. 7.** Bearing power loss test system: (a) high-Speed bearing oil inlet and outlet test bench; (b) schematic diagram of lubrication system oil supply pump; (c) schematic diagram of power transmission path.

of the radial load. One end of the chamber is fitted with a transparent polymethyl methacrylate (PMMA) end cover, which contains uniformly arranged oil injection holes to allow visual monitoring of the oil level, jet behavior, and fluid motion during testing. A return oil port is incorporated at the bottom of the chamber to simulate the complete dynamic oil injection and return process under jet lubrication conditions. An integrated temperature and oil level sensor is embedded in the chamber wall to provide real-time monitoring of the oil height and lubricant temperature in the oil inlet cavity.

To minimize the influence of additional friction on torque measurement, no sealing device is installed between the shaft and the chamber

end cover. The experiments employed a Lanmec ZJ-50A torque speed sensor with a measuring range of ±50 N m torque and maximum rotational speed capability of 6000 r/min, featuring a high accuracy class of ±0.2% of full scale, as shown in Fig. 7(c). This torque sensor is positioned between the input shaft of the test bearing housing and the output shaft of the motor. During testing, a speed and torque sensor collects real-time rotational speed and friction torque data from the test bearing under various operating conditions. The data are transmitted via a torque–speed transmitter to an upper computer system for recording. The test bearing is driven by a 5.5 kW variable-frequency motor, which is set to operate at 100 Hz. The tests aim to simulate oil-jet lubrication conditions without external load; therefore, the test rig is not equipped with additional radial or axial loading capabilities.

Based on the findings of Chen et al. [36], it is reasonable to assume that under extremely low load conditions, the drive system losses and system dry friction losses remain essentially constant and are unaffected by variations in lubricant supply. Building on this premise, the present study first conducted a set of calibration experiments under oil-free conditions prior to formal testing, to determine the baseline resistance torque $T_0$. This torque reflects the combined influence of drive system losses and system dry friction losses at different rotational speeds. Subsequently, formal tests were performed under specified oil immersion conditions, yielding the total resistance torque $T_1$, which includes the drive system losses, system dry friction losses, and the bearing power loss under lubricated conditions. Therefore, the net resistance torque attributable solely to the bearing under oil-jet lubrication can be expressed as:

$$T = T_1 - T_0 \tag{31}$$

Prior to conducting the formal oil-jet lubrication tests, a series of dry-run calibration tests were performed to determine the inherent system resistance torque (baseline) at different rotational speeds. The total resistance torque measured during the subsequent oil-jet lubrication tests was then subtracted by the baseline resistance torque at the corresponding speed. This procedure isolates the net resistance torque attributable solely to lubrication, thereby enabling the accurate determination of the pure lubrication-induced power loss. The oil inlet and return pumps were activated, and after the oil level stabilized, the zero-drift value of the torque sensor was recorded. The motor was then started, with the rotational speed increasing stepwise from 500 r/min to 6000 r/min in increments of 500 r/min. At each speed level, torque data were recorded over a 20-second period after stable operation was achieved. Between two consecutive formal tests, sufficient cooling was applied to the test components and lubricating oil to eliminate the influence of heat accumulation on subsequent results. Each rotational speed condition was tested three times, and the average value was taken as the valid experimental data for that speed point. Finally, by subtracting the results obtained from the calibration tests from the formal test data, additional power losses introduced by non-lubrication factors (such as sealing losses) were eliminated, thereby ensuring the accuracy and reliability of the measured data.

Tables 1 and 2 present the key structural parameters of the bearings used in this study and the main physical properties of the lubricating oil, respectively. To ensure comparability between the experimental results and the theoretical model, the selected bearings must maintain consistency in both the installation interface dimensions and the key parameters affecting theoretical calculations, thereby achieving effective control of variables.

Under conditions without applying additional radial load, high-speed bearing oil-jet lubrication tests were conducted with the initial oil temperature set at 30 °C, an oil flow rate of 2 L/min, a return oil flow rate of 6.9 L/min, a nozzle diameter of 1.5 mm, and the injection direction perpendicular to the bearing end face. With the objective of capturing the resistance torque under stable rotational speeds, the operational temperature rise of the lubricating oil was not considered in this test. To obtain reliable data for each test point, three

**Table 1**
Bearing structural parameters.

| Type | 6206 | NU206 | 30206 |
|---|---|---|---|
| Outer diameter (mm) | 62 | 62 | 62 |
| Inner diameter (mm) | 30 | 30 | 30 |
| Mean diameter (mm) | 46 | 46 | 46 |
| Width (mm) | 16 | 16 | 17.5 |
| Number of rollers | 9 | 19 | 17 |
| Contact angle (°) | 0 | 0 | 14 |

**Table 2**
Lubricant specification table.

| Parameter | Value |
|---|---|
| Kinematic viscosity at 40 °C (cst) | 61.5 |
| Kinematic viscosity at 100 °C (cst) | 9.5 |
| Density at 15 °C (g/cm$^3$) | 0.853 |

sets of repeated measurements were conducted. Data acquisition was performed for 20 s after the torque stabilized, using a 100 Hz sampling rate to acquire 2000 raw data points per set. The raw data were subjected to low-pass filtering to suppress high-frequency noise, and outliers were rigorously removed. Subsequently, the calculated average values were adjusted by subtracting the zero offset of the torque sensor under static conditions, thereby determining the final measurement result for that test point. The directly measured torque–speed data reflect the resistance characteristics only at discrete speed points, which is insufficient to fully characterize the bearing's power loss across the entire operating range. To accurately evaluate the power loss, the measured resistance torque must be converted into the corresponding power loss using the following relationship:

$$P = \frac{1000\,Tn}{9550} \tag{32}$$

where P is power loss, T is resistance torque, and n is rotational speed.

To isolate the independent effects of rotational speed and bearing type on power loss, the experiments were conducted under quasi-steady-state temperature conditions. Specifically, the lubricant temperature was set and maintained at 30 °C using a thermostatic oil tank. Although frictional heating in the bearing could cause temperature variations during oil-jet lubrication, the inlet oil temperature remained essentially constant throughout each measurement period. This was ensured by the short duration of individual data acquisition runs and the large thermal inertia of the system, as the total oil volume in the tank was significantly larger than the circulating flow. Consequently, the power loss data reported in this study were obtained under constant inlet oil temperature conditions, facilitating the direct analysis of mechanical and fluid dynamic mechanisms without the confounding effect of substantial temperature rise.

### 3.2. Comprehensive evaluation of experimental results

As observed from the experimental results in Fig. 8, the power losses of all three bearing types increase with rotational speed, showing consistency with established research findings. Notably, when the rotational speed exceeds 3000 r/min, the power loss of DGBBs increases at a significantly higher rate compared to CRBs and TRBs. Analysis suggests that this discrepancy can be attributed to the following factors:

First, there are fundamental differences in the geometric configuration of rolling elements and contact mechanisms between ball bearings and roller bearings, which directly affect their friction and churning behaviors. Second, significant variations exist in the effective oil volume within the bearing chambers and the efficiency of internal and external oil circulation among different bearing types, consequently influencing the overall level of power losses. Furthermore, existing studies [15] have indicated that power loss under fully flooded lubrication conditions may be lower than that under low oil level conditions.

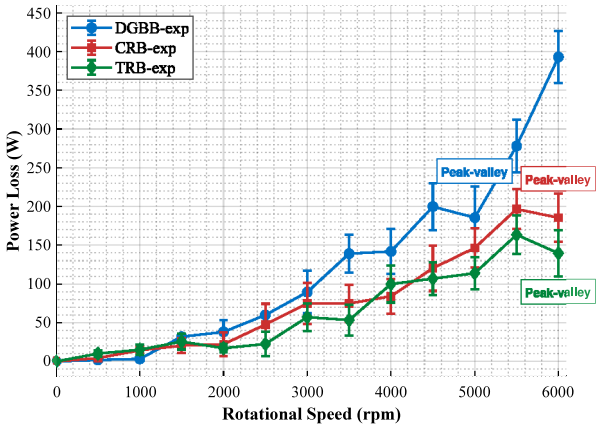


**Fig. 8.** Power loss test data for different bearing types when the oil temperature is 30 ℃: "Peak–valley" indicates anomalous power loss drops at high speeds. (Error bars represent ±1 standard deviation).

Given the same oil supply rate, DGBBs typically exhibit superior oil return capability, resulting in a relatively lower actual oil level within their chambers. Therefore, differences in oil distribution and the resulting variations in churning effects also represent important factors contributing to the observed disparity in power loss growth rates.

When the rotational speed reached 5000 r/min, the power loss of the DGBBs showed a declining trend; while under the 6000 r/min condition, similar phenomena were observed in both CRBs and TRBs. Preliminary analysis suggests that this phenomenon may stem from the transition of the internal flow field within the bearing from laminar to turbulent flow, or from interference caused by coupling resonance in the test system affecting the acquisition accuracy of the sensor.

In numerical modeling research related to power losses in high-speed rolling bearings, Gao et al. [37] systematically analyzed the correlation between the resistance characteristics of rolling elements and the Reynolds number. Their findings indicate that as the Reynolds number increases, the drag coefficient of rolling elements gradually decreases and eventually stabilizes in the high Reynolds number region. With the continuous increase in bearing speed, the Reynolds number of the flow field between raceways correspondingly rises. Under these conditions, the enhancing effect of rotational speed on churning torque may be counteracted by the decreasing drag coefficient, leading to a declining trend in resistance torque. This phenomenon manifests itself as a "peak–valley" characteristic in specific speed ranges within the power loss curve. Furthermore, Gao et al.'s study on the influence mechanism of centrifugal force on oil loss in ball bearings, documented in Ref. [38], provides a reasonable explanation for this anomalous decline in churning torque under specific operating conditions.

The error bands shown in Fig. 8 have been analyzed in terms of their underlying causes. These bands represent the dispersion of multiple repeated test results relative to their mean values at each rotational speed point, primarily arising from the following three factors:

- Measurement System Uncertainty: The inherent accuracy limitations of the torque sensor, combined with mechanical vibration interference during testing, affect signal stability and sensitivity, thereby introducing fundamental measurement errors.
- Variations in Roller Kinematics: Differences in the fluid drag forces acting on the rollers at varying speeds may alter their pure rolling state, introducing sliding friction not fully accounted for in the model. This leads to additional losses and fluctuations in the results.
- Non-uniformity of the Internal Flow Field: As rotational speed increases, the oil-air two-phase flow inside the bearing becomes increasingly complex, making localized oil accumulation, air entrainment, and even cavitation phenomena difficult to avoid. These transient and non-uniform flow characteristics directly influence the actual power loss, contributing to the scatter in the experimental data.

To investigate the source of this deviation, vibration testing was conducted on the test rig spindle. The results indicated the presence of a stable high-frequency vibration component at approximately 1000 Hz, whose acceleration amplitude increased gradually with rotational speed (see Table 3). Analysis suggests that within the 2000–3500 r/min speed range, this high-frequency excitation resonated with the low contact stiffness system of the bearing-induced by the low radial load-thereby significantly amplifying interference with the torque sensor signal and causing abnormal fluctuations in the measured torque readings. This resonant interference is the primary reason for the deviation between experimental data and theoretical predictions in this speed range. At speeds outside this resonance region, the torque signal stabilized, and the consistency between theoretical and experimental results was restored, further validating the effectiveness of the model.

In summary, the above factors collectively constitute the main sources of uncertainty in the experimental results and should be duly considered when analyzing deviations between model predictions and measured data.

## 4. Model validation and discussion

This section systematically compares the theoretical calculations of power loss with experimental data, with a focus on analyzing the impact of the additionally considered loss sources on the total power loss. By evaluating the agreement between theoretical and experimental values at various speed points, the predictive accuracy of the model is assessed, and the causes of deviations in specific speed ranges are discussed, leading to proposed directions for model refinement. Furthermore, the variation patterns of individual loss sources in the theoretical model with respect to rotational speed are examined, and their underlying mechanisms are interpreted within the theoretical framework. Particular emphasis is placed on an in-depth discussion of the speed dependence of the newly introduced loss terms.

### 4.1. Validation of theoretical models

The prediction error range (shaded area) in Figs. 9(a) 9(c) 9(e) is constructed based on the absolute error between the theoretical predictions and the experimental mean values, visually reflecting the overall deviation of the model. In Figs. 9(b) 9(d) 9(f), the numerical ranges of the contribution percentage from each loss source (not experimental intervals) are presented because, with current testing techniques, experiments can only measure the total power loss via a torque sensor and cannot directly and precisely isolate the contribution of each local loss source. Therefore, we employ the theoretical model for mathematical decoupling and calculation to demonstrate the variation trends of individual loss components, which also highlights the analytical value of our model.

Fig. 9(a) indicates that the predictions of the theoretical model generally agree with the experimental data in terms of the overall trend, which is consistent with existing studies [11,12,39]. And which is further supported by a goodness-of-fit ($R^2$) value of 0.9459. For the quantitative assessment, the mean relative error between the predicted values and the experimental data is 32.2%. Further analysis indicates that this discrepancy is attributed primarily to the low-speed operating conditions, where the relatively small power loss leads to a magnified relative error. After excluding the outlier data points in the low-speed region, the mean relative error decreases to 17.1%, demonstrating that the model exhibits satisfactory predictive accuracy within the main operating regime. In the speed range of 0–3000 r/min, the

**Table 3**
Oil-injection lubrication vibration testing.

| Rotational speed (rpm) | 500 | 1000 | 1500 | 2000 | 2500 | 3000 | 3500 | 4000 | 4500 | 5000 |
|---|---|---|---|---|---|---|---|---|---|---|
| Frequency (Hz) | 100 | 100 | 1028.12 | 1031.25 | 1031.25 | 1025 | 993.75 | 950 | 975 | 915.62 |
| Amplitude ($m/s^2$) | 0.51 | 0.51 | 1.10 | 1.15 | 1.96 | 1.86 | 2.13 | 2.9 | 2.62 | 3.1 |

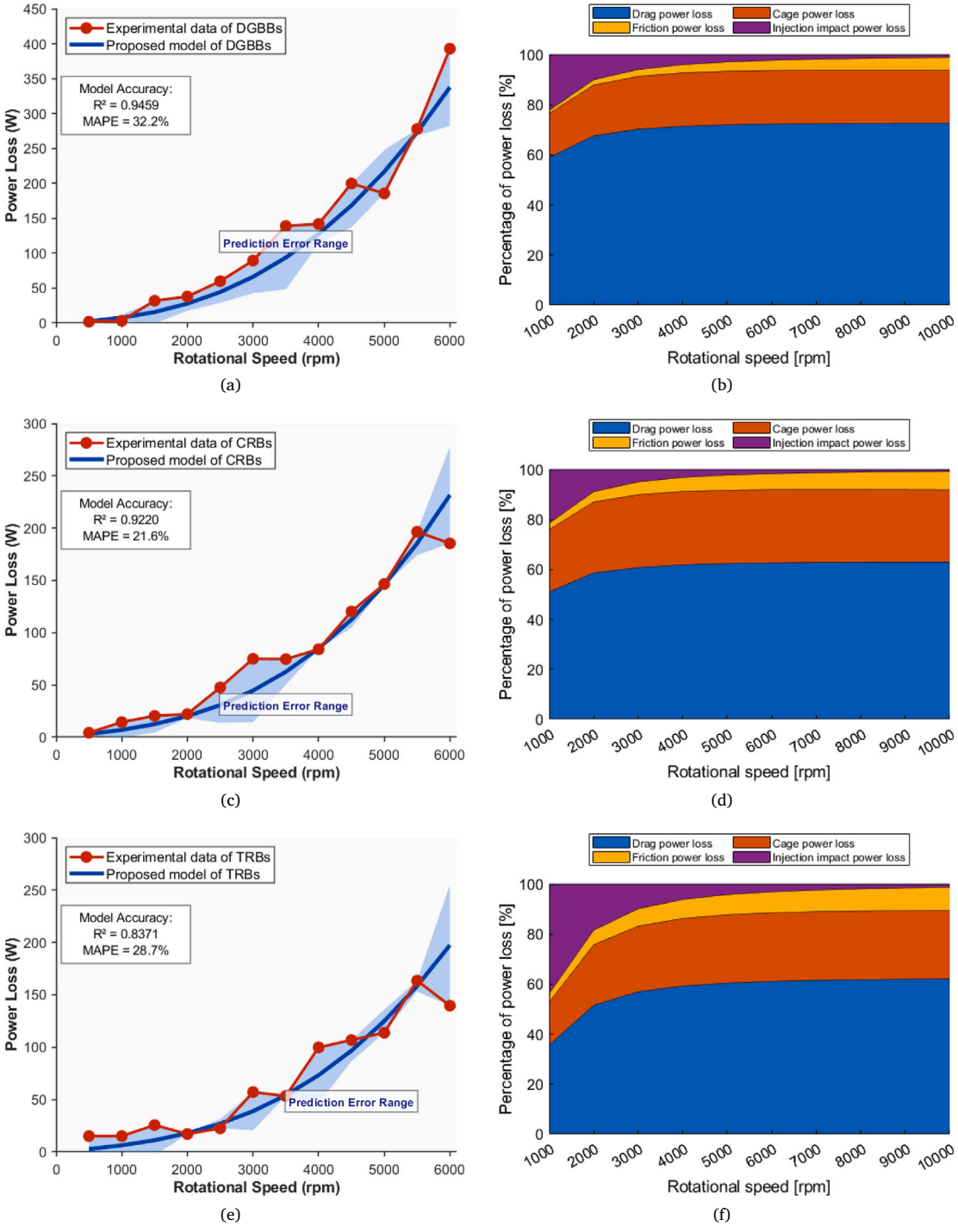


**Fig. 9.** Validation of bearing power loss models (DGBBs: (a), (b), CRBs: (c), (d), TRBs: (e), (f)): theoretical predictions versus experimental data and individual loss source contributions.

theoretical values show good agreement with the experimental results. However, in the higher speed range of 3000–6000 r/min, the model exhibits noticeable underestimation at certain speed points, leading to reduced predictive accuracy. The observed underestimation at high speeds suggests a limitation of the model's constant-viscosity rigid-fluid assumption. With increasing speed and contact pressure [5], the actual

lubricant rheology may deviate from this simplification, highlighting an area for future model refinement.

As can be seen from Fig. 9(b), in the theoretical model results, oil-jet impact loss accounts for a non-negligible proportion of the total power loss when the rotational speed is below 4000 r/min. As the speed increases further, the proportion of this loss gradually decreases. This is primarily because other types of losses grow at a much higher rate with speed than oil-jet impact loss. Additionally, the current impact loss model only considers the kinetic energy dissipation of the lubricant jet in its initial injection direction and does not account for the coupling effect of high-speed bearing rotation on the jet trajectory and energy exchange process. The other three types of losses — fluid drag loss, cage churning loss, and sliding friction loss — all increase with rising speed. Among them, fluid drag loss contributes the most, followed by cage churning loss, with sliding friction loss being the smallest. This distribution characteristic is mainly due to the relatively limited external load applied to the bearing, resulting in a relatively low contribution from sliding friction loss, which is closely related to load.

Fig. 9(c) indicates that the theoretical predictions generally agree with the experimental data in terms of the overall variation trend, which is further supported by a goodness-of-fit ($R^2$) value of 0.9220. Quantitatively, the mean relative error between the predicted and measured values is 21.6%. Further analysis reveals that this error stems mainly from the low-speed region, where the small magnitude of power loss leads to an exaggerated relative error. After excluding outliers in the low-speed range, the mean relative error decreases to 17.4%, indicating that the model achieves good predictive accuracy in the main operating range.

A more detailed comparison across different speed intervals shows that the theoretical values are generally lower than the experimental data in the 0–3500 r/min range. Within this span, the deviation is relatively small from 0 to 2000 r/min but becomes more pronounced between 2000 and 3500 r/min, with the most significant underestimation observed around 3000 r/min. In contrast, good agreement is observed in the 3500–5000 r/min region. The systematic underestimation within the 2000–3500 r/min range corresponds to the vibrational resonance condition identified in Section 3.2 , which introduced significant noise into the torque measurements. In contrast, the good agreement observed outside this resonant range (0–2000 and 3500–5000 r/min) supports the model's predictive capability under stable operating conditions. Fig. 9(d) reveals that the variation patterns of individual loss sources in CRBs are similar to those observed in DGBBs, suggesting a commonality in their loss mechanisms. Therefore, a repeated analysis of these specific trends is deemed unnecessary.

Fig. 9(e) indicates that the theoretical predictions generally agree with the experimental data in the overall variation trend, which is further supported by a goodness-of-fit ($R^2$) value of 0.8371. In the quantitative evaluation, the mean relative error between the two is 28.7%. Further analysis reveals that the error is primarily concentrated in the low-speed operating regime, where the small absolute value of power loss leads to an amplified relative error. After removing the outlier data points in the low-speed region, the mean relative error decreases to 18.4%, demonstrating that the model achieves good predictive accuracy within the main operating range.

The theoretical underestimation for TRBs at low speeds (0–1500 r/min) is likely due to unmodeled frictional losses from axial preload, a common installation constraint for this bearing type. This effect becomes less significant relative to other loss mechanisms as speed increases.

As can be seen from Fig. 9(f), under low-speed conditions at 1000 r/min, oil-jet impact loss accounts for over 40% of the total power loss. Although this phenomenon may be partly attributed to the relatively low contribution of other loss mechanisms at low speeds, it still clearly demonstrates that oil-jet impact loss cannot be overlooked under such operating conditions. While the variation trends of the other three types of losses are generally consistent with those observed in other bearing types, their specific proportional distribution differs compared with DGBBs and CRBs, primarily due to the significant influence of oil-jet impact loss.

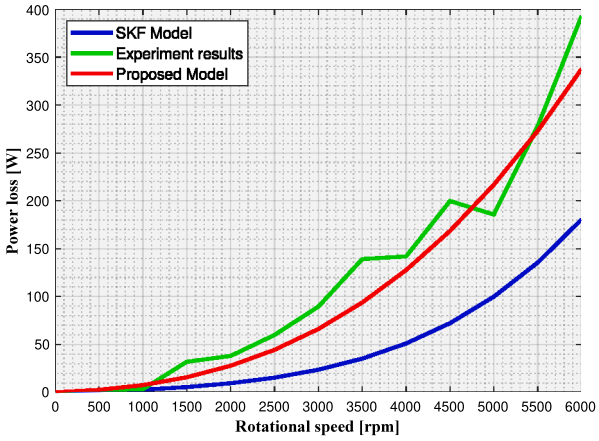


**Fig. 10.** Comparison between the proposed model and the SKF model on DGBBs.

As shown in Fig. 10, in the medium-to-high speed range (>2000 r/min), particularly under the low/no external load oil-jet lubrication conditions that are the focus of this study, the predictive accuracy of the proposed model for power loss is generally superior to that of the SKF model. Specifically, the SKF model exhibits a trend of systematic underestimation within the 1500 to 6000 r/min range. This is primarily because the SKF model, as a global empirical model, fails to adequately distinguish and accurately characterize the complex physical mechanisms dominated by load-independent losses under low-load conditions. In contrast, the localized modeling approach adopted in this study enables the refined quantification of various loss sources such as rolling element drag, jet impingement, and cage churning. Moreover, it specifically incorporates two key mechanisms: the dynamic load effect on rolling elements and the inlet-interface shear loss. Consequently, the proposed model aligns more closely with the actual physical processes in such operating conditions, yielding predictions that are in better agreement with the experimental data.

### 4.2. Inadequately considered loss sources

As shown in Fig. 11, the newly introduced power loss component increases with rotational speed for all three bearing types, yet exhibits distinct variation patterns. The growth in DGBBs is relatively gradual, whereas both CRBs and TRBs show a noticeable increase in slope within the 1000–2000 r/min range, resulting in a steeper upward trend. This discrepancy may be attributed to differences in oil inflow and return characteristics among the bearing types: DGBBs experience a minor decline in dynamically stabilized oil level across speed ranges, while CRBs and TRBs exhibit a more pronounced oil level drop within 1000–2000 r/min (with CRBs showing a greater decrease than TRBs). This leads to a slower growth rate of fluid drag loss compared to that of the newly introduced loss component during this stage, thereby rapidly increasing the proportion of the additional loss in the total loss and manifesting as the significant upward trend observed in figure.

As shown in Figs. 11a–11b, the proportions of $P_s$ and $P_t$ in the total power loss are relatively small at low speeds. As the rotational speed increases, their contributions gradually rise and become non-negligible in the high-speed region. Beyond 8000 r/min, the proportions of both loss components tend to stabilize and become less sensitive to further speed variations. In terms of proportional distribution, the relative contributions of Ps and Pt are higher in CRBs and TRBs than in DGBBs. This indicates that these two loss mechanisms have a more pronounced

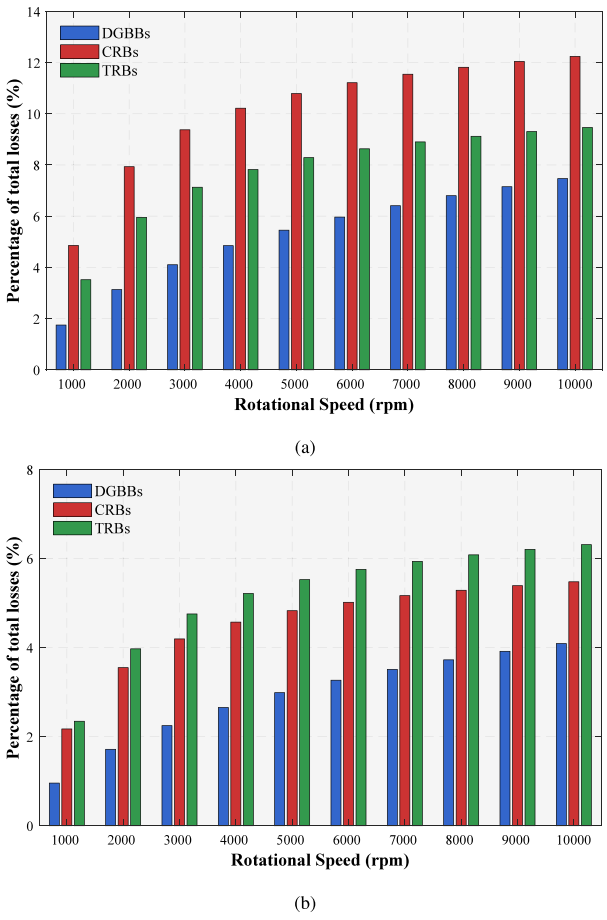


**Fig. 11.** Power loss of inadequately considered loss sources: (a) power loss ($P_s$) due to rolling element dynamic load as a percentage of total loss ($P$), (b) the oil shear drag loss at the bearing inlet interface ($P_t$) of peripheral oil at the inlet interface as a percentage of total loss ($P$).

overall influence on the total power loss prediction for CRBs and TRBs, while their effect is comparatively smaller in DGBBs.

In summary, the incorporation of previously insufficiently considered loss sources has positively improved the power loss prediction for all bearing types. Particularly in the medium to high-speed range, it enhances the consistency between the model and experimental results, thereby strengthening the model's completeness and engineering applicability.

### *4.3. Summary*

Before summarizing the main findings, it is necessary to acknowledge the limitations inherent in the modeling approach.

The model is built upon the core assumption of pure rolling contact between rolling elements and raceways. However, under the low radial load conditions employed in the experiments, the normal load in the contact zone is relatively small, which consequently lowers the maximum available traction force to sustain pure rolling. Under such conditions, slip of the rolling elements may occur [8]. This slip introduces additional power loss mechanisms not captured by the present model. Consequently, this limitation may lead to an underestimation of the total power loss by the model.

Based on the comparative results Fig. 8, it can be concluded that the theoretical model established in this study cannot yet accurately predict certain specific anomalous conditions observed in the experiments. These deviations largely stem from complex disturbing factors present in the actual test environment. To enhance the model's adaptability to real operating conditions, subsequent research could incorporate CFD simulations to refine the modeling of local flow field characteristics and anomalous phenomena, thereby compensating for the limitations of the theoretical model.

Furthermore, regarding the distribution proportion of each loss source, beyond 5000 r/min, the variation trends gradually stabilize, indicating that the power loss structure becomes essentially steady in this range and rotational speed is no longer the dominant influencing factor. To further validate the model's general applicability and strengthen its persuasiveness, follow-up studies could systematically examine the model's response characteristics under different lubrication conditions by varying operational parameters such as oil inlet flow rate or oil temperature.

The findings from this model provide direct insights for the design and selection of bearings in helicopter transmission systems. Under the high-speed, low-radial-load conditions representative of cruise operations, the dominance of load-independent losses highlighted in this study necessitates a shift in bearing selection criteria—from solely load-capacity-based to one that also prioritizes low fluid dynamic resistance. For instance, the greater high-speed loss observed in DGBBs compared to CRBs and TRBs (Fig. 8) underscores the importance of internal flow management in bearing design for efficiency-critical applications. Additionally, the significant contribution of the two supplemented mechanisms ($P_s$ and $P_t$) at high speeds provides a more accurate basis for predicting power loss in transmission systems, enabling better thermal management and lubrication design from the outset.

Future research should expand the scope of experimental validation to include various bearing types and a broader range of operating conditions, thereby further validating the model's utility in aerospace and other high-speed transmission applications. To improve model accuracy, a pressure–viscosity correction term could be introduced to address current underestimation deviations. Additionally, the influence of different structural dimensions on bearing performance should be incorporated to extend the model's geometric applicability. Furthermore, combining CFD methods for refined simulation of the internal flow field in bearings would help to more accurately reveal local loss mechanisms, thereby continuously improving the model's completeness and engineering applicability.

## 5. Conclusion

Motivated by the power loss challenges in helicopter transmission systems, this study develops a general theoretical model to predict the power loss of high-speed rolling bearings under oil-jet lubrication. The model aims to support bearing selection and optimize lubrication design for such demanding applications. To enhance physical completeness, the model incorporates two key mechanisms: the dynamic load effect on rolling elements and the oil shear dissipation at the inlet zone. The model was validated using a dedicated test rig under a low radial load condition, which is typical for such systems yet acknowledges a limitation to the model's universality. Results indicate that the theoretical predictions align well with experimental data in overall trends. Further analysis reveals the variation of individual loss components with rotational speed and highlights the contribution of the newly added loss terms. The main conclusions are as follows:

- The power loss composition is strongly speed-dependent below 6000 r/min but stabilizes at higher speeds. Deep groove ball bearings exhibit greater high-speed loss than roller bearings, primarily due to differences in internal oil distribution and churning effects.
- The inclusion of the two supplemented mechanisms provides a necessary physical correction, significantly enhancing the model's predictive accuracy at medium to high speeds, particularly for cylindrical and tapered roller bearings.

- The main limitation stems from the pure-rolling assumption under low load, which may lead to underestimation. Future work should extend validation to broader loads, integrate pressure–viscosity effects, and employ CFD for refined flow analysis.

In summary, rooted in the application context of helicopter transmissions, this study provides a generalized modeling framework with improved physical fidelity for predicting bearing power loss under oil-jet lubrication with low radial load. It offers a theoretical basis for informed bearing selection and the suppression of inefficient power dissipation in high-speed transmission systems, with immediate relevance to helicopter engineering.

## CRediT authorship contribution statement

**Pengfei Zhou:** Writing – original draft, Investigation. **Jie Ling:** Writing – review & editing, Supervision, Investigation, Funding acquisition. **Ruifeng Zhao:** Writing – review & editing, Investigation, Data curation.

## Declaration of competing interest

The authors declare that they have no known competing financial interests or personal relationships that could have appeared to influence the work reported in this paper.

## Data availability

The data that has been used is confidential.

## References


[1] Yu Q, Gao W, Gong P, Li Y, Li C. Oil distribution around ball–raceway local contact region in under-race lubrication of ball bearing. Dynamics 2024;4(3):731–46. http://dx.doi.org/10.3390/dynamics4030036.

[2] Jiang L, Liu Z, Huang W, Lyu Y, Li Y, Zhang C. Sensitivity analysis and optimization on oil capture performance of under-race lubrication system for high-speed bearings. Tribol Int 2024;195:109598. http://dx.doi.org/10.1016/j.triboint.2024.109598Actions.

[3] Tu W, Wang H, Liu C, Hu D, Yu W. Influence of temperature on dynamic contact characteristics of oil-jet lubricated rolling bearings. Proc Inst Mech Eng K 2024;238(2):167–81. http://dx.doi.org/10.1177/14644193241257207.

[4] Pinel SI, Signer HR, Zaretsky EV. Comparison between oil-mist and oil-jet lubrication of high-speed, small-bore, angular-contact ball bearings. Tribol Trans 2001;44(3):327–38. http://dx.doi.org/10.1080/10402000108982465.

[5] Zhao Y, Zi Y, Chen Z, Zhang M, Zhu Y, Yin J. Power loss investigation of ball bearings considering rolling-sliding contacts. Int J Mech Sci 2023;250:108318. http://dx.doi.org/10.1016/j.ijmecsci.2023.108318.

[6] Jones A. Ball motion and sliding friction in ball bearings. J Basic Eng 1959;81(1):1–12. http://dx.doi.org/10.1115/1.4008346.

[7] Palmgren A. Ball and roller bearing engineering. Philadelphia: SKF Industries Inc; 1959.

[8] Harris TA. Rolling bearing analysis. 3rd ed.. John Wiley & Sons; 1991.

[9] Bakolas V, Roedel P, Koch O, Pausch M. A first approximation of the global energy consumption of ball bearings. Tribol Trans 2021;64(5):883–90. http://dx.doi.org/10.1080/10402004.2021.1946227.

[10] de Cadier de Veauce F, Marchesse Y, Touret T, Changenet C, Ville F, Amar L, Fossier C. Power losses of oil-bath-lubricated ball bearings—a focus on churning losses. Lubricants 2024;12(11):362. http://dx.doi.org/10.3390/lubricants12110362.

[11] Darul L, Touret T, Changenet C, Ville F. Power losses of oil-jet lubricated ball bearings with limited applied load: Part 1—theoretical analysis. Tribol Trans 2023;66(5):801–8. http://dx.doi.org/10.1080/10402004.2023.2235400.

[12] De Cadier de Veauce F, Darul L, Marchesse Y, Touret T, Changenet C, Ville F, Amar L, Fossier C. Power losses of oil-jet lubricated ball bearings with limited applied load: Part 2—experiments and model validation. Tribol Trans 2023;66(5):822–31. http://dx.doi.org/10.1080/10402004.2023.2235395.

[13] Zhou R, Hoeprich M. Torque of tapered roller bearings. J Tribol 1991;113(3):590–7.

[14] Rivera G, Po PJ, Kang C-s, Hong S-W. Analytical formulation for sliding friction torque in cylindrical roller bearings. J Mech Sci Technol 2024;38(9):4669–82. http://dx.doi.org/10.1007/s12206-024-0805-6.

[15] Peterson W, Russell T, Sadeghi F, Berhan MT. Experimental and analytical investigation of fluid drag losses in rolling element bearings. Tribol Int 2021;161:107106. http://dx.doi.org/10.1016/j.triboint.2021.107106.

[16] Feldermann A, Fischer D, Neumann S, Jacobs G. Determination of hydraulic losses in radial cylindrical roller bearings using CFD simulations. Tribol Int 2017;113:245–51. http://dx.doi.org/10.1016/j.triboint.2017.05.015.

[17] Liebrecht J, Si X, Sauer B, Schwarze H. Investigation of drag and churning losses on tapered roller bearings. Strojniški Vestnik-J Mech Eng 2015;61(6):399–408. http://dx.doi.org/10.5545/sv-jme.2015.2490.

[18] Zhao R, Zhou P, Zhong J, Yang D, Ling J. A comparative investigation of CFD approaches for oil–air two-phase flow in high-speed lubricated rolling bearings. Machines 2025;13(8):678. http://dx.doi.org/10.3390/machines13080678.

[19] Marchesse Y, Changenet C, Ville F. Drag power loss investigation in cylindrical roller bearings using CFD approach. Tribol Trans 2019;62(3):403–11. http://dx.doi.org/10.1080/10402004.2018.1565009.

[20] Maccioni L, Chernoray VG, Concli F. Investigating lubricant behavior in a partially flooded tapered roller bearing: Validation of a multiphase CFD solver for aerated oil sump via particle image velocimetry studies and high-speed camera acquisitions. Tribol Int 2025;201:110274. http://dx.doi.org/10.1016/j.triboint.2024.110274.

[21] Hu S, Gong W, Xu X, Liu X. Modeling of ball bearing churning losses. Phys Fluids 2024;36(8). http://dx.doi.org/10.1063/5.0219694.

[22] Chen J, Wu B, Zhu X, Yang C, Zhang Y, Huang X, Dai Y. Multi-objective optimization of air-oil two-phase flow for helicopter planetary gear bearings based on the kriging surrogate model and NSGA-II algorithm. Eng Appl Comput Fluid Mech 2025;19(1):2559098. http://dx.doi.org/10.1080/19942060.2025.2559098.

[23] Kim K-S, Lee D-W, Lee S-M, Lee S-J, Hwang J-H. A numerical approach to determine the frictional torque and temperature of an angular contact ball bearing in a spindle system. Int J Precis Eng Manuf 2015;16(1):135–42. http://dx.doi.org/10.1007/s12541-015-0017-1.

[24] Hong S-W, Tong V-C. Rolling-element bearing modeling: A review. Int J Precis Eng Manuf 2016;17(12):1729–49. http://dx.doi.org/10.1007/s12541-016-0200-z.

[25] Liu J, Xu Z. An optimization design method of a cylindrical roller bearing with the low friction torque. J Tribol 2022;144(11):111201. http://dx.doi.org/10.1115/1.4054671.

[26] Zhu W, Zhu R, Tang X, Lu F, Bai X, Wu X, Li F. CFD-based analysis of oil and gas two-phase flow characteristics in double-row tapered roller bearings with different rib structures. Appl Sci 2022;12(3):1156. http://dx.doi.org/10.3390/app12031156.

[27] Chen H, Liang H, Wang W, Zhang S. Investigation on the oil transfer behaviors and the air-oil interfacial flow patterns in a ball bearing under different capillary conditions. Friction 2023;11(2):228–45. http://dx.doi.org/10.1007/s40544-021-0592-3.

[28] Schlichting H, Gersten K. Boundary-layer theory. Springer; 2016.

[29] Isbin H, Sher NC, Eddy K. Void fractions in two-phase steam-water flow. AIChE J 1957;3(1):136–42. http://dx.doi.org/10.1002/aic.690030122.

[30] Zhao R, Ling J, Zhou P, Zhong J, Yang D. Analytical modeling and experimental validation of gear churning loss in helicopter transmission lubrication systems. J Tribol 2026;148(1):014601. http://dx.doi.org/10.1115/1.4069431.

[31] Jia F, Wang B, Fu Y. A novel prediction model for churning power loss of spur gear. Lubr Sci 2024;36(8):645–55. http://dx.doi.org/10.1002/ls.1721.

[32] Houpert L. Ball bearing and tapered roller bearing torque: analytical, numerical and experimental results. Tribol Trans 2002;45(3):345–53. http://dx.doi.org/10.1080/10402000208982559.

[33] Li X, Liu J, Huang S, Pan G. Friction moment calculation method for tapered roller bearings under combined loads. Sci China Technol Sci 2024;67(8):2565–78. http://dx.doi.org/10.1007/s11431-024-2705-6.

[34] Parker RJ. Comparison of predicted and experimental thermal performance of angular-contact ball bearings. Tech. rep., NASA Technical Reports Server; 1984.

[35] Gupta PK, Gibson HG. Real-time dynamics modeling of cryogenic ball bearings with thermal coupling. J Tribol 2021;143(3):031201. http://dx.doi.org/10.1115/1.4047582.

[36] Chen S-W, Matsumoto S. Influence of relative position of gears and casing wall shape of gear box on churning loss under splash lubrication condition—some new ideas. Tribol Trans 2016;59(6):993–1004. http://dx.doi.org/10.1080/10402004.2015.1129568.

[37] Gao W, Lyu Y, Liu Z, Nelias D. Validation and application of a numerical approach for the estimation of drag and churning losses in high speed roller bearings. Appl Therm Eng 2019;153:390–7. http://dx.doi.org/10.1016/j.applthermaleng.2019.03.028.

[38] Gao W, Nelias D, Lyu Y, Boisson N. Numerical investigations on drag coefficient of circular cylinder with two free ends in roller bearings. Tribol Int 2018;123:43–9. http://dx.doi.org/10.1016/j.triboint.2018.02.044.

[39] Darul L, Touret T, Changenet C, Ville F. Power loss analysis of an oil-jet lubricated angular contact ball bearing: theoretical and experimental investigations. Lubricants 2024;12(1):14. http://dx.doi.org/10.3390/lubricants12010014.